ELSEVIER

Contents lists available at ScienceDirect

International Journal of Biological Macromolecules

journal homepage: www.elsevier.com/locate/ijbiomac





Reduced graphene oxide influences morphology and thermal properties of silk/cellulose biocomposites

Abneris Morales ^a, Sneha Seelam ^a, Stacy A. Love ^a, Sean M. O'Malley ^{a,c}, Xiao Hu ^{d,e}, David Salasde la Cruz ^{a,b,*}

- a Center for Computational and Integrative Biology, Rutgers University, Camden, NJ, United States of America
- ^b Department of Chemistry, Rutgers University, Camden, NJ, United States of America
- ^c Department of Physics, Rutgers University, Camden, NJ, United States of America
- ^d Department of Physics and Astronomy, Rowan University, Glassboro, NJ, United States of America
- e Department of Biomedical Engineering, Rowan University, Glassboro, NJ, United States of America

ARTICLE INFO

Keywords: Cellulose Semi-crystallinity β-Sheet Reduced graphene oxide Morphology Conductivity

ABSTRACT

In recent decades, research into biomaterials such as silk or cellulose has rapidly expanded due to their abundance, low cost, and tunable morphological as well as physicochemical properties. Cellulose is appealing due to its crystalline and amorphous polymorphs while silk is attractive due to its tunable secondary structure formations which is made up of flexible protein fibers. When these two biomacromolecules are mixed, their properties can be modified by changing their material composition and fabrication methodology, e.g., solvent type, coagulation agent, and temperature. Reduced graphene oxide (rGO) can be used to increase molecular interactions and stabilization of natural polymers. In this study, we sought to determine how small amounts of rGO affect the carbohydrate crystallinity and protein secondary structure formation as well as physicochemical properties and how they affect overall ionic conductivity of cellulose-silk composites. Properties of fabricated silk and cellulose composites with and without rGO were investigated using Fourier Transform Infrared Spectroscopy, Scanning Electron Microscopy, X-Ray Scattering, Differential Scanning Calorimetry, Dielectric Relaxation Spectroscopy, and Thermogravimetric Analysis. Our results show that addition of rGO influenced morphological and thermal properties of cellulose-silk biocomposites, specifically through cellulose crystallinity and silk β -sheet content which further impacted ionic conductivity.

1. Introduction

Biocomposites made from proteins and polysaccharides have excellent biocompatibility as well as mechanical properties with applications not only in the biomedical field but also in the energy field [1]. One promising application for biomaterials is their use as bio-electrolyte membranes [2–5]. However, despite many promising aspects in different fields of interest, there remains a lack of understanding of natural polymer morphology in relation to its physicochemical properties.

Protein-polysaccharide blended films interact via hydrogen bonds, hydrophobic-hydrophilic interactions, and electrostatic interactions. These interactions form a matrix where the material's properties will depend on the polymer composition, coagulation solutions, and type of solvent [2]. Cellulose is a natural polysaccharide widely used in research

due to its abundance, biocompatibility, hydrophilicity, low toxicity, and biodegradability [6–10,32,35]. It is constructed of a linear homopolysaccharide composed of repeating D-glucose units and is synthesized in the plant's cell wall via membrane-spanning synthase complexes [2,3,6,8,9,11,32,35]. Its structure contains glycosidic linkages between glucose units at the C1 and C4 positions [12,32,35]. Cellulose is stabilized via hydrogen bonds and van der Waals forces, thus, exhibiting strong intermolecular and intramolecular hydrogen bonding. These inter- and intramolecular forces can also facilitate the formation of films, fibers, or hydrogels through physical crosslinking [3,6–8,10,32,35]. Cellulose contains crystalline and amorphous regions, with the interchain hydrogen bonding being responsible for its crystalline properties [10,13,32,35]. As a biomaterial, cellulose has some disadvantages such as a poor mechanical performance, e.g., high stiffness, and is insoluble in many typical organic solvents due to his highly ordered structure

^{*} Corresponding author at: Center for Computational and Integrative Biology, Rutgers University, Camden, NJ, United States of America. E-mail address: ds1191@camden.rutgers.edu (D. Salas-de la Cruz).

[3,8,12,13,17].

In an effort to modify some of the properties of cellulose, we generated composites of cellulose and a protein. The protein of choice for this investigation is silk fibroin due its versatility as a biomaterial and great solubility with polysaccharides [1]. Silk is obtained from a variety of organisms that include spiders and silkworms [14,15]. It is one of the most explored proteins due to its exceptional mechanical properties, controlled biodegradability, ease of processing, and excellent biocompatibility [1,3-5,14,16]. Bombyx mori silk, a naturally occurring silk from the Bombyx mori silkworm, is made of repeating glycine, alanine, and serine amino acids in the sequence, (GAGAGS)_n. Its strands are naturally coated with sericin which can be chemically removed [3-5,13,15,16]. Due to its repeating amino acid composition, silk can form highly specific anti-parallel β-sheet structures, providing it with crystalline regions and other secondary structures [13,16]. When silk is blended with cellulose, hydrogen bonds and electrostatics interactions add new properties and ameliorate existing undesired properties such as high stiffness [3].

For this study, an ionic liquid, 1-ethyl-3-methylimidazolium acetate (EMIMAc), was employed to facilitate the blending process. Ionic liquids (ILs) have been used extensively for the dissolution of natural polymers due to their unique properties such as low toxicity, chemical/thermal stability, high ionic conductivity, reusability, non-flammability, and their ability to not produce unwanted byproducts [1,3,6,17,18,35]. ILs also provide enhancements to polymer dissolution which facilitates biocomposite formation [13]. ILs are molten salts that consist of bulky, unsymmetrical ions with a delocalized charge where the cation carries chemical characteristics and the anion provides solution stability [1,3,12,35]. EMIMAc was chosen for this study because of its inclusion of an imidazolium ring which offers low viscosity and stability [1,35]. The dissolution of cellulose in ionic liquids proceeds through a disturbance of cellulose's hydrogen bonds caused by the IL's ions interactions of the IL with the hydroxyl groups of cellulose. Silk undergoes a similar dissolution process involving disturbance of hydrogen bonds among its amino acid groups [3-6,16]. Once the natural polymers have been added to the IL, they will begin to associate with the salt ions via hydrogen bonding, and hydrophobic, hydrophilic, and electrostatic interactions [5]. This process involves a diffusion of the IL molecules into the cellulose fibers, which then causes the cellulose fibers to swell and disentangle between the cations and anions [19]. A similar phenomenon occurs with silk. However, to allow for this dissolution process to begin, the hydrogen bond network of cellulose must first be eliminated so that the hydroxyl groups can disassociate from the cellulose backbone [12,19]. After successful dissolution, the blended polymer solution is submerged in a coagulation agent to diffuse the ions now embedded within the biopolymer matrix [4]. The introduction of a coagulation agent into the blended polymer matrix leads to phase separation, resulting in formation of the composite [4,5]. While the coagulation process aims to remove the IL from the final composite, a trace amount of IL remains entrapped in the blend and influences the ionic conductivity of the overall biocomposite [4,5]. The remaining amount of ionic liquid trapped provides the required concentration of free ions, which are influenced by ion hopping and the segmental motion of the blended material to induce ion conduction [20,21]

Graphene oxide is a modified graphene sheet that contains oxygen functional groups and exhibits strong mechanical strength, thermal/electrical conductivity, and has a large surface area [6,7,22,23]. Graphene oxide can be thermally or chemically reduced to obtain rGO. In this investigation, vitamin C was utilized in the chemical reduction of graphene oxide to rGO. The augmented surface of rGO contains functional groups such as hydroxyls, epoxides, and carbonyls. Such functional groups provide solubility properties in polar solvents, exhibit moderate biocompatibility, and serve as an intermediary for sites to link other macromolecules and rGO [6,10,22]. In this study rGO was used as an additive to investigate morphological changes that in turn affect physicochemical properties and overall ionic conductivity of the

blended films. The creation of new naturally conductive materials such as the films discussed in this study, can provide 'green' alternatives for use in various industries and applications [5]. It has been previously shown that the ionic conductivity of silk/cellulose is dependent on the protein β -sheet content, IL type, and coagulant bath type [4,5]. There have also been previous studies which showed successful formation of hydrogels by combining wood pulp dissolved in 1-butyl-3-methylimidazolium chloride and rGO [7]. Here, a modified version of these biocomposites was used, in which silk and cellulose were blended with EMIMAc and regenerated with three different agents: water, a solution of 10 % ethanol, and a solution of 10 % hydrogen peroxide. The aim of this study was to understand the variations in morphological and physicochemical properties of silk/cellulose biocomposites, and how these variations affect the ionic conductivity of the polymer systems with the addition of rGO.

2. Materials and methods

2.1. Ionic liquid

1-Ethyl-3-methylimidazolium acetate (95 %) was obtained from Sigma-Aldrich. As pretreatment, the IL was heated in a vacuum oven at a pressure of 30 inHg and a temperature of 50 $^{\circ}\text{C}$ for 24 h for the removal of water residues.

2.2. Silk

Bombyx mori silk cocoons were obtained from Treenway Silks in Lakewood, CO. To remove the sericin coating on the silk fibers, the cocoons were boiled for 15 min in a $0.02~{\rm NaHCO_3}$ (Sigma-Aldrich) solution. This process was then followed by rinsing the fibers with deionized water three times to assure complete removal of the sericin coating. The fibers were left to dry overnight followed by placement in a vacuum oven at room temperature with a pressure of 30 inHg to ensure removal of moisture.

2.3. Cellulose paper

Cytiva Qualitative Grade Plain Filter Paper Circles and Sheets, grade P4 manufactured from cellulose fibers, were purchased from Fishersci (cat no. 09-803-6E). The filter paper was cut into small pieces to facilitate dissolution.

2.4. Reduced graphene oxide

Graphene oxide dispersed in $\rm H_2O$ was obtained from Sigma-Aldrich (SKU: 763705-25ML) and was reduced using 0.005 g vitamin C in 1 mL of distilled water. The agitated solution was heated in an oil bath at 50 °C for 24 h and was subsequently washed 5 times via centrifuge to assure removal of vitamin C residues. The solution was then filtered through a pre-measured cellulose filter paper and left to dry at room temperature for 72 h. Incorporated rGO accounted for 1 % of the total mass of the cellulose paper.

2.5. Dissolution of the cellulose paper and the silk

The pretreated ionic liquid was measured to account for 90 % of sample total mass, with silk and the cellulose paper accounting for 10 % of the total mass, of which cellulose paper accounted for 40 % and silk accounted for 60 %. The measured ionic liquid was pipetted into a vial and heated in a silica oil bath at a temperature of 85 $^{\circ}$ C. The silk was cut and frayed into smaller pieces prior to dissolution. After all silk was dissolved, cellulose paper was added piecewise to the solution. This mixture was left to agitate for 24 h at 85 $^{\circ}$ C.

2.6. Preparation of the biofilm

A 1 mL pipette tip was placed in an oven at 75 °C for 10–15 min. With the pre-heated pipette tips, the silk/cellulose solution was pipetted into 12 mm \times 12 mm \times 1 mm polylactic acid 3D printed molds. The molds were subsequently placed in a beaker containing 100 mL of the selected coagulation agent and sealed with parafilm. This coagulation phase lasted for 48 h at room temperature for optimal IL removal. Afterwards, the molds were removed from their baths and rinsed with distilled water 3 times to remove IL residues. The molds were then placed in a Teflon Petri dish and stored in a low-pressure desiccator. Prior to analysis the samples were placed in a vacuum oven for 24 h to remove any atmospheric moisture. Digital images of final films that contain rGO can be seen in Fig. S-1.

2.7. Fourier transform infrared spectroscopy (FTIR)

A Bruker (Billerica, MA, ISA) ALPHA-Platinum ATR-FTIR Spectrometer with a Platinum-Diamond sample module was used to obtain spectroscopy data of the films. Before each sample measurement, background was collected consisting of 128 scans. For the analysis of the samples 32 sample scans were carried out at 6 different sample locations with a resolution of 4 cm⁻¹ per each scan. Spectra were reported between 4000 cm⁻¹ to 400 cm⁻¹. Opus 7.2 software was used for data manipulation and analysis. A Fourier self-deconvolution was utilized to study the amide I regions located between 1595 cm⁻¹ and 1705 cm⁻¹, and a Lorentzian line shape was used with parameters of a 25.614 cm⁻¹ half-band width along with a noise reduction factor of 0.3. Gaussian profiles were employed for fitting results and in the integration in order to find the area that corresponded to a specific wavelength. The data were normalized for visualization purposes.

2.8. Thermogravimetric analysis

Thermogravimetric measurements were obtained using the TA Instrument (New Castle, DE, USA) Discovery TGA system. 5 mg samples were purged in a nitrogen gas chamber with a flow rate of 25 mL/min. Each run started at 30 °C and underwent an isothermal period of 1 min. Then the system was ramped up to 600 °C at a constant rate of 10 °C/min. Subsequent to data acquisition, a step transition analysis was used to calculate the temperature onset $(T_{\rm o})$ and temperature end $(T_{\rm f})$ of decomposition as well as the percent of total weight loss. For each sample the fastest rate of change in weight loss as a function of temperature (ΔT_p) was calculated and reported. For visualization purposes, the thermograms are shown as negative derivatives.

2.9. Differential scanning calorimetry

Differential Scanning Calorimetry data were obtained utilizing a TA Instrument differential scanning calorimeter which is furnished with a refrigerated cooling system. A nitrogen flow of 50 mL/ min was applied to the chamber during data acquisition. Each sample weighed 5 mg and was placed in an aluminum Tzero pan. The procedure for each sample was as follows: equilibration at $-40\,^{\circ}\text{C}$, modulate 0.318 $^{\circ}\text{C}$ every 60 s, an isothermal period of 3 min, end of cycle, a ramp of 2.00 $^{\circ}\text{C}/\text{min}$ to 400 $^{\circ}\text{C}$, end of cycle.

2.10. Scanning electron microscopy

Topographical analysis of samples was obtained utilizing a JEOL JCM-6000 Scanning Electron Microscope. Each sample was coated by a Denton Desk II sputter coater with Au—Pt to mitigate surface charge buildup. Samples were allowed to dry after coating for best image resolution. Each image was obtained at a magnification of $500\times$; scale-bar length is $100~\mu m$.

2.11. X-ray scattering

Morphology of films was assessed with the help of a Xeuss 2.0 Dual Source Environmental X-ray Scattering system located at the University of Pennsylvania. CuK α , $\lambda=0.154$ nm, was used for incident radiation, and a slit size at high flux, 1.2 mm \times 1.2 mm, was used for data acquisition with a time-run of 600 s per sample. The films were taped to a general sample holder and placed inside the chamber under vacuum. Although both SAXS and WAXS were obtained, only WAXS is presented in this report. With the use of Foxtrot 3.4.9 to evaluate the x-ray profiles, azimuthal integration was used to obtain intensity versus scattering vector q profiles.

2.12. Dielectric relaxation spectroscopy

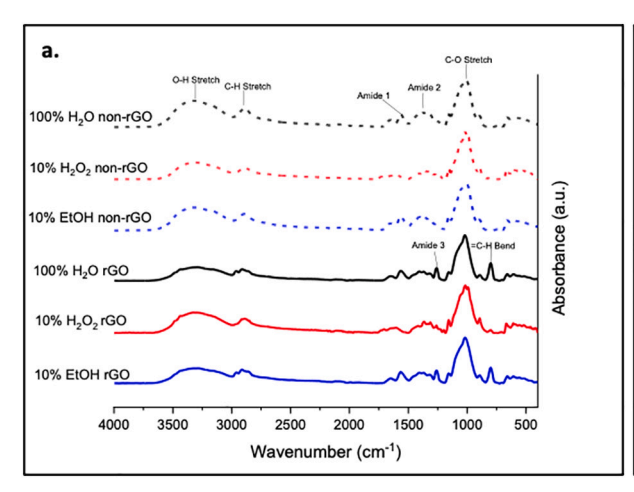
Dielectric Relaxation Spectroscopy (DRS) was used to determine the ionic conductivity of the biocomposites. Ionic conductivity of the films was measured using a Solartron Analytical Materials Lab XM and a Janis ST-100 Optical Cryostat. The films were placed between two copper electrodes with a diameter of 5 mm and were heated under vacuum within a temperature range of 450–300 K. The measurements consisted of sweeping the frequency from 0.1 Hz to 1 MHz at 10 K intervals starting at 450 K.

3. Results and discussion

3.1. Infrared spectroscopy

Fourier Transform Infrared Spectroscopy was utilized to ensure that the films were blended properly. Normalized data in Fig. 1a show absorbance peaks representative of cellulose at 1180–930 cm⁻¹ (C-O-C stretch), 3000-2750 cm⁻¹ (C-H stretch), 3600-3000 cm⁻¹ (O-H stretch) [31,35]. Absorption peaks for silk appear at 1720–1600 cm⁻¹ and 1590–1500 cm⁻¹ which represent the amide I and amide II regions of silk, respectively. Appearance of these peaks reveals that the biocomposites are well blended and the final product is a composition of both silk and cellulose. Data are analyzed to understand if morphology changes as a function of coagulation type and/or as a function of the presence or absence of rGO. As a function of coagulation baths, the amide I and II regions start to shift for biofilms regenerated in hydrogen peroxide, which can be confirmed by examining the data shown in Fig. 1b. There are no significant differences in the spectrograms of films regenerated in ethanol or water. In the presence of rGO, we see an appearance of the amide III region at 1250 cm⁻¹. Unlike the amide I band, a water peak does not interfere with the protein's amide III band and also shows resolved individual bands allowing for a better and more reliable secondary structure analysis [24]. There is also an appearance of a =C-H bending mode at 760 cm⁻¹. This peak could be an aromatic, specifically ortho substitute, as rGO is a polycyclic aromatic hydrocarbon.

Analysis of the protein's secondary structure was performed by manipulating the data with Fourier Transform Deconvolution at the amide regions shown in Fig. 1b to calculate the percentages of side chains, β -sheets, random coils, alpha helices, and turns. Table 1 show values for the effects of both the composition and coagulation type on secondary structure of the biocomposites. Previous work has demonstrated that the addition of GO changes the protein β -sheets structure of proteins [30]. In this study the presence of rGO increases the β -sheet content, which is correlated with the crystalline regions of the protein, when compared to films without rGO. Also, there is an increase in β -sheet content for the films coagulated in hydrogen peroxide. Specifically, the films that contain rGO have the highest percentage of β -sheets. This can be attributed to silk chains forming more β -sheet in the presence of rGO and hydrogen peroxide.



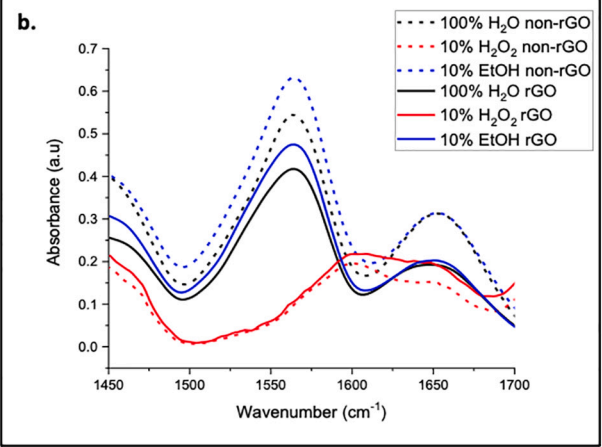


Fig. 1. (a) Combined FTIR data for 60 % silk and 40 % cellulose biofilms with and without the addition of reduced graphene oxide. (b) The combined data for the amide regions.

Table 1Secondary structure percentages for 60 % silk and 40 % cellulose biofilms with and without the addition of rGO.

Composition	Coagulant	Side chains	Beta sheets	Random coils and alpha helices	Turns
Non-rGO	100 % H ₂ O	0.42	21.1	44.6	33.9
Non-rGO	$10 \% H_2O_2$	2.49	24.4	38.7	34.4
Non-rGO	10 % EtOH	0.23	19.7	47.3	32.7
rGO	100 % H ₂ O	0.36	28.7	40.7	30.2
rGO	$10 \% H_2O_2$	5.19	30.4	58.3	6.10
rGO	10 % EtOH	0.22	23.7	35.8	40.3

3.2. Thermogravimetric analysis

Fig. 2 shows thermograms for films with and without rGO as well as the derivatives that were utilized to obtain the maximum temperatures of decomposition. It has been previously found that the thermograms for pure cellulose and silk samples, are more stable than blended films and exhibit a unimolecular derivative peak [31]. Beginning with the films that did not contain rGO, films coagulated in hydrogen peroxide demonstrated overall greater thermal stability, while the films coagulated in water demonstrated the weakest thermal stability (Table 2). The non-rGO films coagulated in hydrogen peroxide obtained the lowest weight loss percentage which means that these films were able to maintain more weight during thermal decomposition. In contrast, the non-rGO films coagulated in water had the highest weight loss percentage. The maximum temperature $(T_{\Delta max})$ denotes the largest change of the samples weight as a function of temperature (Fig. 2b). The films coagulated in hydrogen peroxide were the most thermally stable, having the greatest increase in temperature and were thus better able to withstand thermal decomposition longer. All of the non-rGO film thermograms demonstrated a bimodal feature. The bimodal decomposition arises from the different morphological regions within the films. Interfaces of amorphous regions degrade first followed by the crystalline regions [25]. This can be seen in Fig. 2b, for example the higher derivative peak in the bimodal thermograms is correlated to the amorphous regions in the non-rGO films degrading more quickly than the crystalline regions. The fast degradation of the amorphous regions plays a key role in the thermal stability of the film. When relating thermal stability of the films to their protein secondary structure content, nonrGO films coagulated with hydrogen peroxide had the highest β -sheet content and thus had the highest thermal stabilities. This indicated that the crystalline regions within a film provide enhanced structural and thermal stability. The films coagulated with water were shown to be the least thermally stable relative to all samples. Analysis of secondary structures showed that films coagulated with water were mainly composed of turns and random coils. Therefore, films coagulated in water are more amorphous, resulting in lower thermal stability. The films coagulated in ethanol follow a similar trend to the films coagulated in water. This means that ethanol did not have substantive effects on the thermal stability of non-rGO films. The peak that is located at 100 °C is due to water retention of the samples. We further confirmed that the peak located at 100 °C was not due to IL decomposition since EMIMAc has a decomposition temperature that is greater than 200 °C (Fig. S-2). It is important to note that it has been previously shown in separate thermal data of the individual polymers that silk and cellulose do not contain similar water retention peaks [31]. Blessing et al. reported the appearance of a similar evaporation peak appears at 100 °C. In that study, they correlated water absorbance to semi-crystallinity in which polymer blends with higher cellulose content retained less water; however, polymers blended with higher silk content had higher water retention [5]. In another study from Blessing et al., films coagulated in hydrogen peroxide had greater water retention peaks than films coagulated in other solvents. These findings by Blessing et al. correspond with our observations in Fig. 2b and d [4]. Therefore, we denote these peaks at 100 °C as water retention peaks which form due to the silk content within the films and/or type of coagulation agent used.

The thermograms of films with rGO and coagulated in hydrogen peroxide have overall greater thermal stability while films coagulated in ethanol have the weakest thermal stability. The thermal stability of our films is determined from the onset temperature in Table 2. We note that, previously, thermal data has shown that the addition of IL decreases the onset temperature of the cellulose-IL films [35]. From onset temperatures in Table 2, we conclude that the films coagulated in ethanol have a comparatively low thermally stability. Furthermore, plots of all films with rGO in Fig. 2d show a bimodal derivative. However, two of the films (ethanol and hydrogen peroxide) contain a smaller initial derivative peak. This peak can be attributed to a small portion of the films degrading at that temperature. Higher temperatures were needed to fully degrade the films coagulated in ethanol and hydrogen peroxide. In terms of secondary structures, ethanol and hydrogen peroxide reduce creation of amorphous regions resulting in higher crystallinity of the films. In the films coagulated in ethanol the largest derivative peak is located at the same position as the initial derivative peak of the films coagulated in water. This can be due to amorphous regions in the ethanol-coagulated films degrading first followed by the crystalline

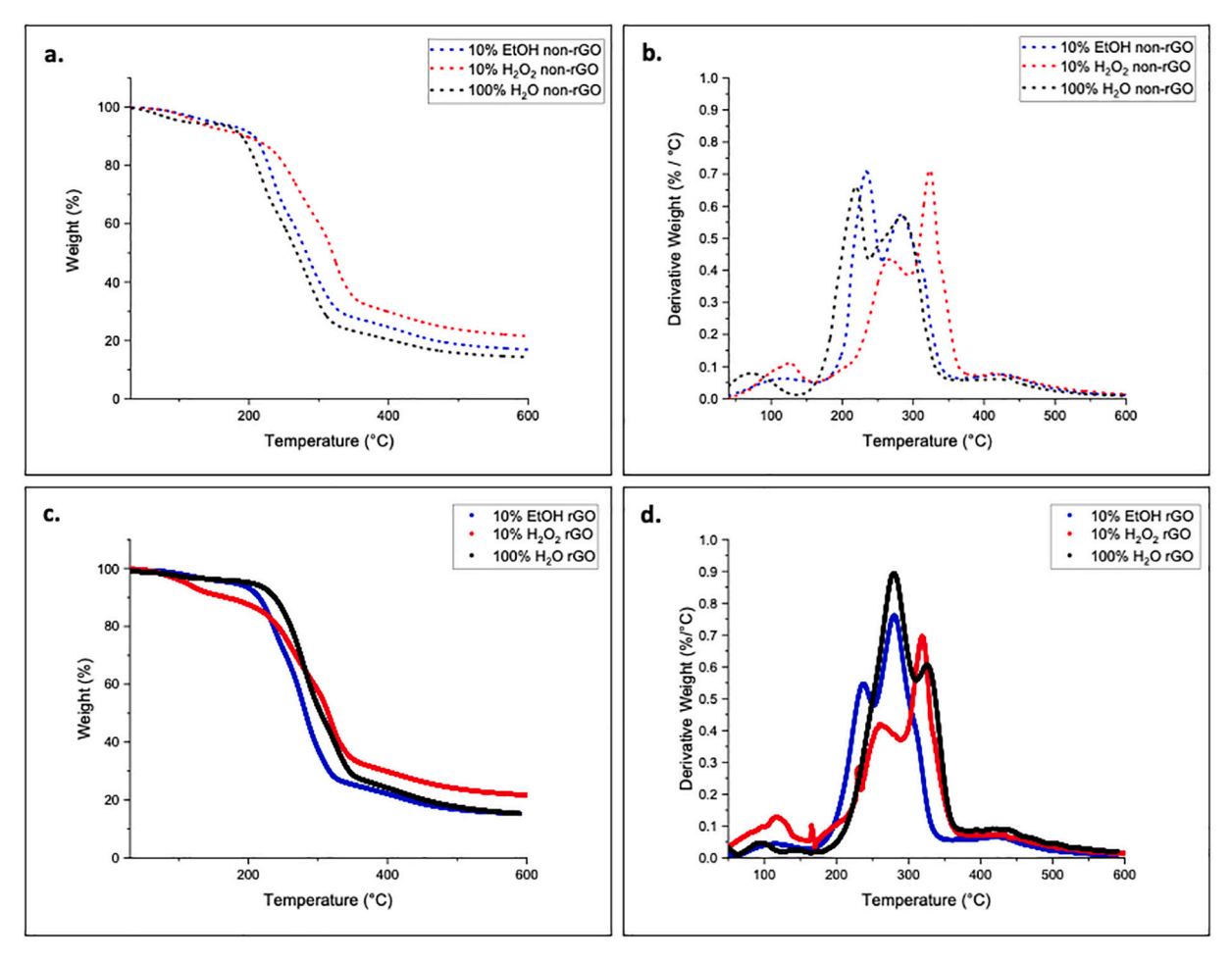


Fig. 2. (a) Thermal analysis data obtained from TGA of 60 % silk and 40 % cellulose biofilms that did not contain reduced graphene oxide. (b) The derivative of the thermogram as a function of coagulation agent. (c) Thermal analysis data of films that did contain reduced graphene oxide, and (d) the corresponding derivative as a function of coagulation agent.

Table 2 Results obtained from thermal data which depict the onset temperature of degradation (T_{onset}), the end temperature of degradation (T_{end}), percent loss of the film (Wt. Loss %), and the rate of change as a function of temperature ($T_{\Delta max}$).

· Directo					
Composition	Coagulant	T _{onset} (°C)	T _{end} (°C)	Wt. loss (%)	$T_{\Delta Max}$ (°C)
Non-rGO	100 % H ₂ O	193.2	293.4	71.4	219.2,
					284.7
Non-rGO	$10 \% H_2O_2$	258.6	355.5	78.8	266.4,
					324.4
Non-rGO	10 % EtOH	214.2	298.3	68.1	233.9,
					283.4
rGO	$100 \% H_2O$	229.9	344.8	71.6	277.4,
					325.6
rGO	10 % H ₂ O ₂	258.3	350.9	78.7	261.1,
					318.6
rGO	10 % EtOH	215.0	308.5	74.2	237.4,
					280.1

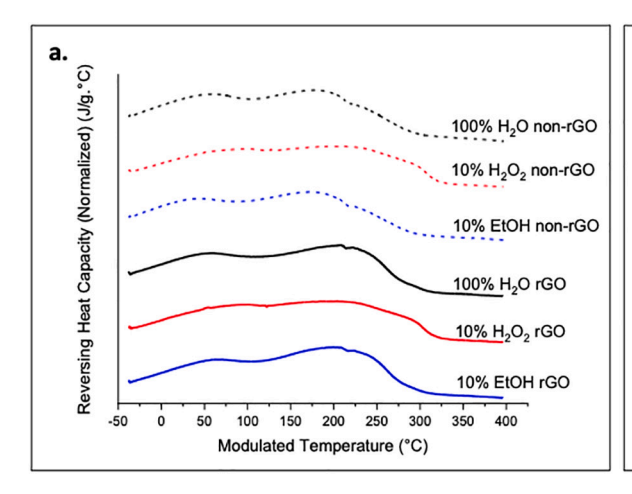
regions. The X-ray scattering data provides additional insight into the effects of coagulation agent and rGO content on film crystallinity and morphology.

3.3. Differential scanning calorimetry

Differential scanning calorimetry (DSC) scans were collected in a continuation of the thermal analysis (Fig. 3a-b). Glass transition

temperatures were obtained from the reversing heat capacity scans and the exothermic (crystallization) peaks. Endothermic peaks were obtained from the total heat flow scans. All values are shown in Table 3. Among non-rGO films, those coagulated in ethanol exhibited the lowest glass transition temperature at 111.2 °C (384.35 K), and the films coagulated in hydrogen peroxide had the highest glass transition temperature, 140.0 °C. Similar to TGA data, the films coagulated in ethanol and water were not significantly different from each other; their respective glass transition temperatures were only separated by 4.5 °C. Films coagulated in hydrogen peroxide did not have an endothermic peak, however, they showed an exothermic peak at 106.4 °C (379.55 K). This peak corresponds to crystallization occurring at that specific temperature. The films coagulated in water and ethanol show two exothermic peaks starting at 210.2 °C (483.35 K) and 204.4 °C (477.55 K) respectively. As demonstrated in the TGA data in Table 2, onset temperatures of degradation begin at approximately 200 °C. Comparatively, in Fig. 3, there are exothermic peaks that are present at 229.7 °C and 295.9 °C, 300.6 °C and 261.1 °C, and 291.4 °C, respectively, for water, hydrogen peroxide, and ethanol films with rGO (Table 3). These peaks appear after the start of degradation denoted by the TGA thermograms. Therefore, these exothermic peaks are due to film degradation. We note is that the exothermic peaks for water and ethanol film are very similar to one another, however, the films coagulated with hydrogen peroxide differ in their degradation data. This points to differences in morphology between the biocomposites associated withtheir solvents used for coagulation.

Among films not containing rGO (non-rGO), coagulation in hydrogen



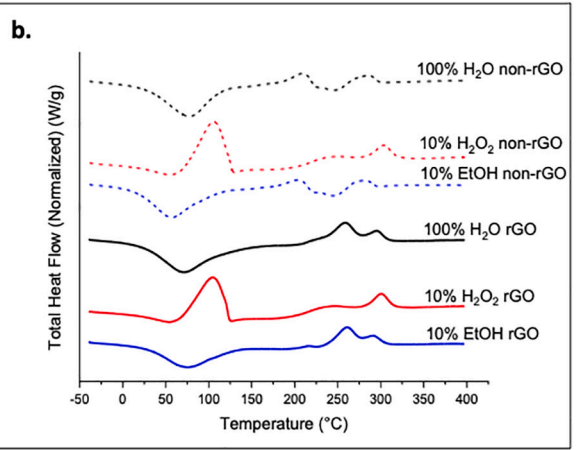


Fig. 3. Data obtained from DSC of 60 % silk and 40 % cellulose biofilms with and without the addition of reduced graphene oxide. (a) The total heat flow vs temperature and (b) reversing heat capacity vs modulated temperatures as a function of coagulation agent.

 $\begin{tabular}{ll} \textbf{Table 3} \\ \textbf{The glass transition temperatures, degradation temperatures, and crystallinity temperatures of all films.} \end{tabular}$

Composition	Coagulant	T _g (°C)	T _g (K)	Endothermic peak	Exothermic peaks
Non-rGO	100 % H ₂ O	115.7	388.8	78.1	210.2, 232.4, 288.5
Non-rGO	10 % H ₂ O ₂	140.0	413.2	-	106.4, 302.9
Non-rGO	10 % EtOH	111.2	384.3	56.4	204.4, 229.7, 278.6
rGO	100 % H ₂ O	131.6	404.7	70.3	257.3, 295.9
rGO	10 % H ₂ O ₂	138.7	411.8	-	104.8, 300.6
rGO	10 % EtOH	132.6	405.7	75.8	217.6, 261.1, 291.4

peroxide resulted in the highest glass transition temperature (138.7 °C), while the film coagulated in water had the lowest glass transition temperature (131.6 $^{\circ}$ C, 404.75 K). In regards to the exothermic peaks that appear at 232.4 and 288.5, 302.9, 229.7 and 278.6 for the water, hydrogen peroxide, and ethanol films without rGO, respectively, these occur after the start of degradation according to the TGA onset temperatures in Table 2. In both rGO and non-rGO films, the exothermic peaks present for the water and ethanol films are similar to each other, while the profile of the hydrogen peroxide films differ from the water and ethanol's profiles. The films coagulated in water and ethanol exhibit similar trends, as their glass transition temperatures differ only by 1 °C, thus, indicating that water and ethanol did not significantly affect their glass transition temperatures. In contrast, the film coagulated in hydrogen peroxide without rGO had greater thermal stability. In terms of DSC, the non-rGO film coagulated in hydrogen peroxide also had a higher glass transition temperature. This indicates that hydrogen peroxide affects at least one of the natural polymers considering that in the β-sheet content analysis, the films coagulated in hydrogen peroxide

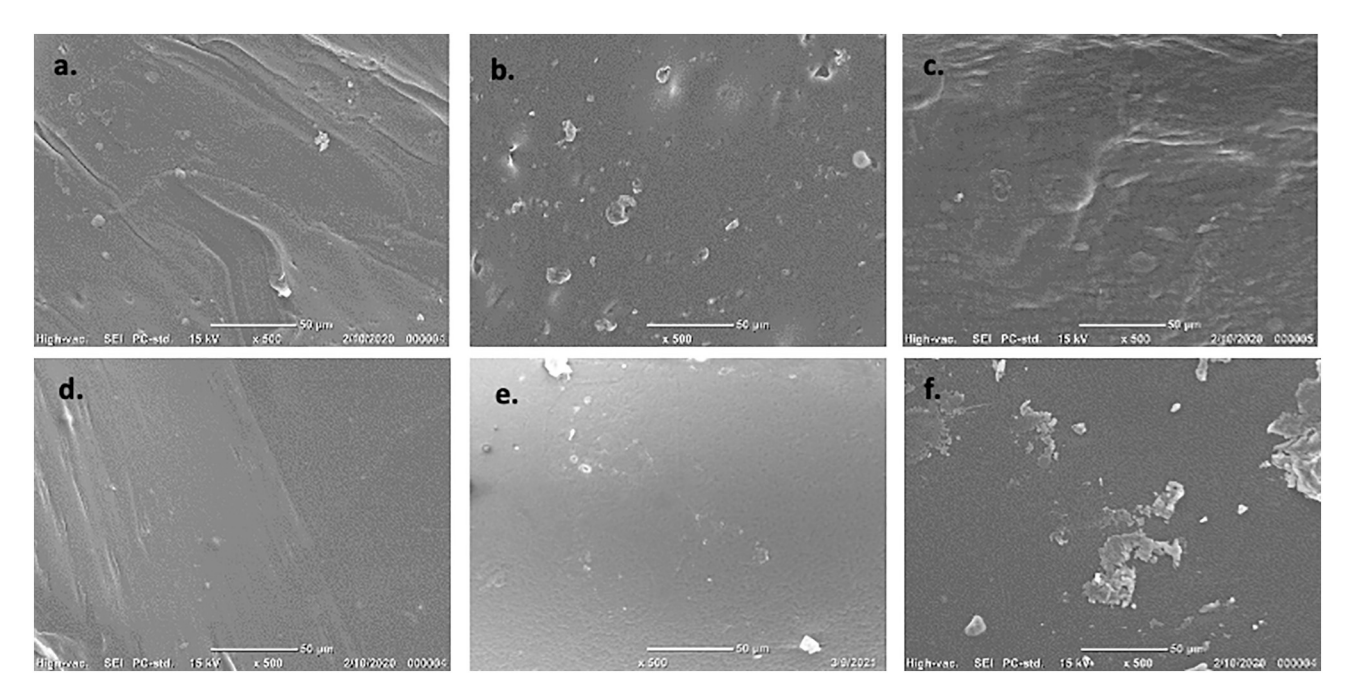


Fig. 4. Scanning electron images of 60 % silk and 40 % cellulose films. The first row is the films that contain rGO: a. 10 % ethanol, b. 10 % hydrogen peroxide, and c. 100 % water. The second row does not contain rGO: d. 10 % ethanol, e. 10 % hydrogen peroxide, and f. 100 % water.

also had greater β -sheet content. Nonetheless, both rGO and non-rGO films coagulated in hydrogen peroxide showed similar trends, only differing by a few degrees. Furthermore, the addition of rGO seemed to modify the thermal properties of the films, specifically, increasing the glass transition temperature for most composites.

3.4. Scanning electron microscopy

Scanning Electron microscopy (SEM) was used to study the topographical properties of the rGO and non-rGO films (Fig. 4). Overall, images of films show uniformity and homogeneity. For both rGO and non-rGO films, those coagulated in ethanol look mostly smooth. However, images of rGO films have small specks on the surface, and when coagulated in ethanol, show more topographical folding in the upper right corner. Furthermore, the image of the film coagulated with hydrogen peroxide and containing rGO showed greater "roughness" than other films. However, when coagulated in hydrogen peroxide, films without rGO exhibit the most visually smooth surfaces (Fig. 4e). The film coagulated in water with rGO exhibited many spheres and bumps that appeared to be underneath the surface of the sample, and for the film coagulated in water without rGO appeared smooth but with "specks" on its surface. Overall comparison of the rGO and non-rGO samples revealed that the non-rGO films were topographically smoother with further contrast resulting from the effects of the coagulation methods. In the supplemental information, we have included images of the fabricated rGO-based biocomposites (Fig. S-1).

3.5. X-ray scattering

Morphological analysis was conducted on silk and cellulose biofilms to observe and compare the structural changes caused by different fabrication methods, such as the inclusion of rGO and varying the coagulation agents. Wide-angle scattering data of the biofilms were analyzed between 5° and 35° in the 2θ range (Fig. 5). Analysis of the results demonstrated no major morphological differences between the films with or without rGO although the film coagulated in ethanol showed an additional scattering peak. Throughout the dissolution process, IL will transform the morphology of cellulose from cellulose I $_{\rm I}$ to cellulose II or cellulose III [32,34,35]. Cellulose II, it is more structurally stable than cellulose due to its anti-parallel arrangement [28,34]. Cellulose III, which is derived from either cellulose I or cellulose II, has intra-chain hydrogen bonding that is similar to cellulose II but has parallel cellulosic chains [28,32,34]. Prior investigations have shown that cellulose filter papers exhibit diffraction peaks at $2\theta = 14.7$ °,

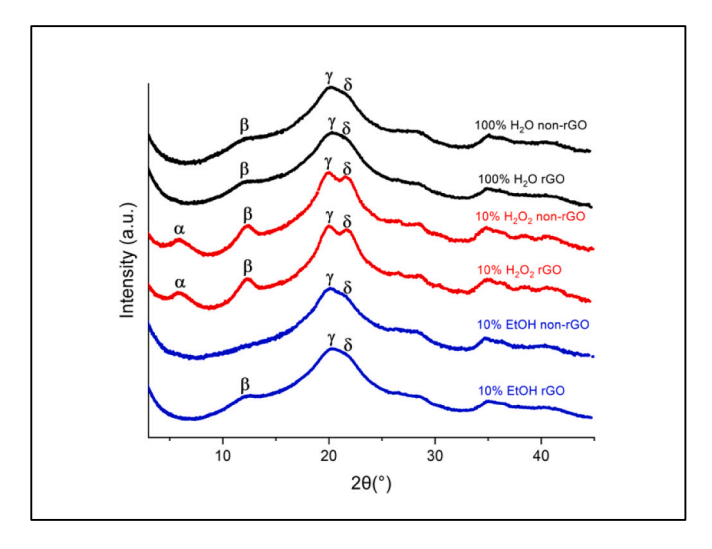


Fig. 5. Normalized wide-angle X-ray scattering data for 60 % silk and 40 % cellulose samples with and without the addition of reduced graphene oxide.

16.8 °, and 22.7° in which corresponds to the crystalline planes (101), (10-1) and (002) respectively [29,33–35]. These values are characteristic of monoclinic cellulose I [29,33–35]. Pure silk fibers exhibit diffraction peaks at $2\theta=20.5$ °, 17.8°, 9.3°, and 3.7 [4,31]. Differences in the silk and cellulose blended films coagulated in hydrogen peroxide in this study showed characteristics of a semi-crystalline morphology representative of cellulose II [32]. This observation indicated a selective interaction of hydrogen peroxide molecules interacting with cellulose within the biofilm matrix during fabrication [2,26]. Films coagulated in ethanol and water had an overall amorphous morphology and changes in morphology corresponded to an increase in the contrast between silk and modified cellulose [4,31,32].

The interplanar spacing, or d-spacing, was calculated using the following equation, $d=\frac{2\pi}{q}$ (Table 4). The crystal sizes of biofilms were also calculated in order to obtain a deeper understanding of the biofilm crystallization trends. The Scherrer equation, $\tau = \frac{K\lambda}{\beta \cos \theta}$, was utilized to obtain values where τ is the average size of the crystallites, K is the Scherrer constant (0.94), λ is the wavelength of the x-ray beam (with a value of 0.154 nm), β is the full width half maximum (FWHM), and $\cos\theta$ is the Bragg angle also known as the angle located between the primary beam and the family of lattice planes. All values are noted in Fig. 6. The films coagulated in hydrogen peroxide have the highest calculated crystal size at 3.82 nm for rGO and 3.68 nm for non-rGO films. As mentioned earlier, this is a result of the selective interaction between cellulose and hydrogen peroxide where the crystal morphology of the cellulose is influenced within the biofilm matrix [2,26]. Among the biocomposites containing rGO, the crystal size decreased by 0.40 (when coagulated in 10 % ethanol), and by 0.50 (when coagulated in water) at ~20.00°. However, in films coagulated with hydrogen peroxide the crystal size increase by 0.14 in the presence of rGO. A similar trend was observed for the peak at ~22.00°. For films coagulated in water and ethanol, inclusion of rGO in the biofilm matrix correlated with a reduced crystal size. For films coagulated in hydrogen peroxide, the crystal size was unaffected by the presence of rGO, and these crystals remained the largest at 4.96 nm. Overall, however, the addition of rGO reduced the crystal size. This is expected as rGO incorporates anchor points for hydrogen bonds throughout the cellulose backbone. From these findings we conclude that the presence of rGO influences the morphology of the biocomposite system; however, as seen in the films coagulated in hydrogen peroxide, the main driver of film morphology is the interaction between coagulation agent and cellulose.

3.6. Ionic conductivity

Ionic conductivity of the films is shown in Fig. 7a-b. The relationship $\sigma = L/AR$ was utilized to calculate the conductivity where L is the distance between the two electrodes, A is the cross-sectional area of the electrodes, and R is taken as the low frequency x-intercept of the Nyquist plot [27]. The dominant mechanism observed in these polymer systems is believed to be ion hopping. The ionic conductivity of similar polymer systems containing silk, cellulose, and IL have been previously studied. In that study, it was found that the interaction of the IL with the polymer chains, along with changes in morphology including β -sheet formation, can hinder or enhance the overall ionic conductivity of the films [4,5].

In this study, the glass transition temperatures obtained from DSC analysis influenced the overall ionic conductivity of the biofilms. The ionic conductivity data were normalized to remove the influence of the glass transition temperature observed in Fig. 8b. The films coagulated in ethanol and water displayed an Arrhenius behavior such that the conductivity trends were linear in the log-log plot. The ionic conductivity of films that did not contain rGO decreased by two orders of magnitude with respect to their non-rGO counterparts as a function of coagulation agent (Fig. 7a). The films coagulated in hydrogen peroxide showed lower conductivity in comparison to the films coagulated in ethanol. With the addition of rGO, films coagulated in ethanol and water

Table 4
Values of the wide-angle X-ray scattering peaks for the 60 % silk and 40 % cellulose samples with and without the addition of reduced graphene oxide.

Sample	α	α		β		γ		δ	
	q (nm ⁻¹)	d (nm)							
10 % EtOH rGO	_	_	8.93	0.70	14.33	0.44	15.54	0.40	
10 % EtOH non-rGO	_	-	_	_	14.20	0.44	15.36	0.41	
10 % H ₂ O ₂ rGO	4.27	1.47	8.70	0.72	14.12	0.44	15.44	0.41	
10 % H ₂ O ₂ non-rGO	_	-	8.85	0.71	14.18	0.44	15.48	0.41	
100 % H ₂ O rGO	_	-	8.70	0.72	14.60	0.43	15.49	0.40	
100 % H ₂ O non-rGO	-	_	8.76	0.72	14.25	0.44	15.45	0.41	

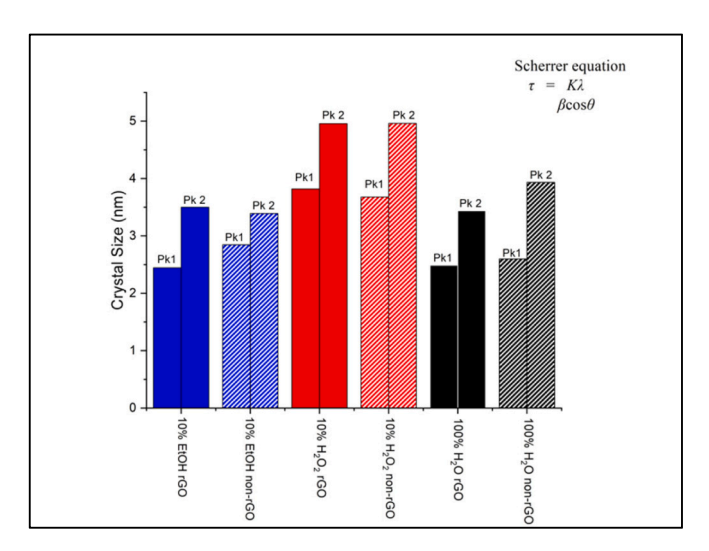


Fig. 6. Crystal size calculation results demonstrating the difference between the two peaks of the 60% silk and 40% cellulose biofilms with and without the addition of reduced graphene oxide.

displayed reduced conductivity, which indicates that the presence of rGO disrupts ion mobility. However, in the case of films coagulated with hydrogen peroxide, the addition of rGO aids in increasing ionic conductivity of the overall polymer system. In the morphology studies, we reported that cellulose tends to interact with hydrogen peroxide, which influences the crystallinity of the overall film [2,26]. Since the interaction between cellulose and hydrogen peroxide is preferred due to their strong hydrogen bonding interactions, ions prefer to interact with the amorphous or less crystalline regions of the matrix. This is due to the tightly packed cellulose-hydrogen peroxide matrix that inhibits the

ability of ions to move swiftly through its matrix. This interaction decreases the ionic conductivity of the hydrogen peroxide films. The samples coagulated with hydrogen peroxide also showed high β -sheet content and enhanced crystallite size, which further leads to low ionic conductivity. Normalized conductivity plots for films coagulated in either water or ethanol did not differ substantively.

The schematic in Fig. 8 illustrates the morphological and physicochemical effects on the biomaterials of regeneration with hydrogen peroxide. With the addition of hydrogen peroxide, there is an increase in the cellulose crystallites, demonstrated in Figs. 5 and 6. Addition of rGO increases the percentage of β -sheets structure as demonstrated in Table 1. These effects influence the ionic conductivity. There is an apparent correlation between β -sheet content and enhanced ionic conduction. Blessing et al. showed that there is a relationship between ionic conductivity and β -sheet content wherein the ionic conductivity correlates positively correlated with β -sheet content in a silk and cellulose system [4,5].

4. Conclusion

We successfully integrated reduced graphene oxide into silk-cellulose films and observed key morphological and physicochemical changes. The characterization tests conducted produced intriguing information on the morphology, structure, and ionic conductivity of these biofilms. From FTIR, we were able to determine that all polymeric components were successfully blended. FTIR was also vital in calculating the secondary structural content of the films, where it was observed that the presence of rGO enhanced β -sheet content. These findings indicate that rGO influences the structural integrity of the composites. Furthermore, the resulting films obtained a homogeneous topography. This finding is linked to the thermal analysis (TGA) data which showed that the films with rGO had higher onset temperatures than the composites without rGO. Furthermore, DSC studies indicated

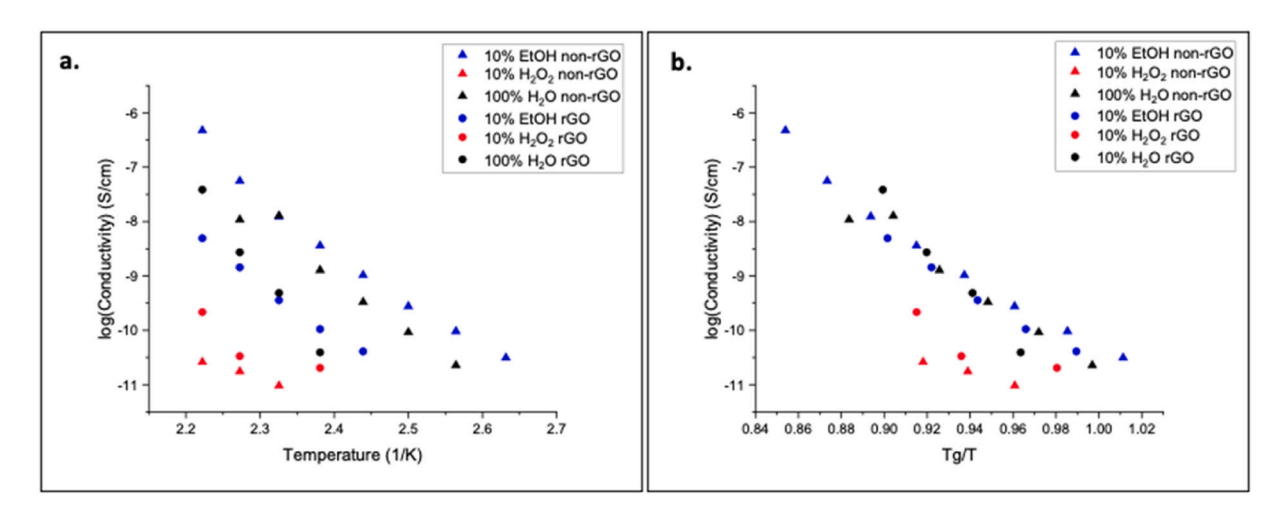


Fig. 7. (a) Data obtained using a cryostat to measure the conductivity of 60 % silk and 40 % cellulose films with and without reduced graphene oxide. (b) Glass transition temperature divided by the temperature of conductivity measurement.

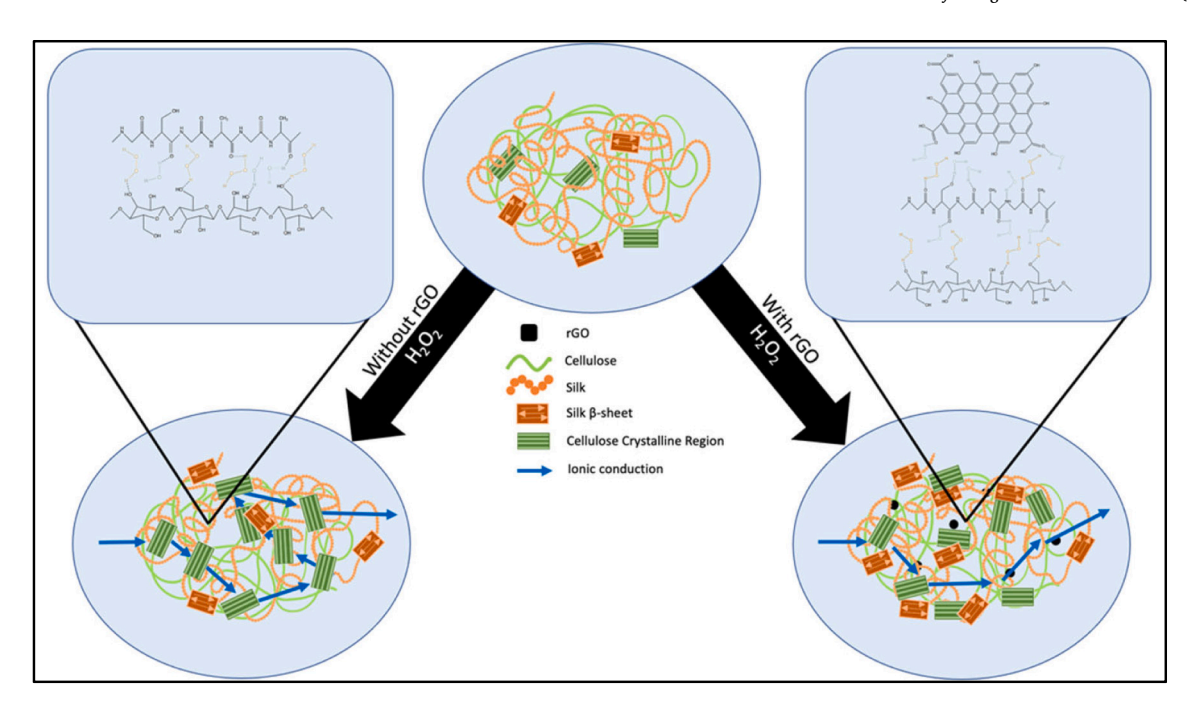


Fig. 8. Morphological changes in a cellulose silk system mixed with and without rGO and coagulated in hydrogen peroxide.

that films without rGO are reported had a lower glass transition temperature than films with rGO. Thus the addition of rGO increased the glass transition temperature of the films and changed film morphology. In contrast, the presence of rGO negatively affected the overall ionic conductivity of the film, which resulted in a less conductive biofilms due to changes in the biocomposite morphology. However, rGO did improve ionic conductivity of films coagulated in hydrogen peroxide. To explain why conductive trends were different for films coagulated in hydrogen peroxide, X-ray scattering data showed that inclusion of hydrogen peroxide produced a semi-crystalline morphology, whereas inclusion of ethanol or use of water alone resulted in an overall amorphous morphology. The semi-crystalline morphology of films coagulated with hydrogen peroxide is related to the hydrogen bonding interaction between cellulose and hydrogen peroxide during the coagulation stage, which leads to a tightly bonded matrix. Ions present in the hydrogen peroxide and cellulose matrix thus favor interaction with the silk polymer chains rather than the cellulose, resulting in higher ionic conduction. As shown by our data from the hydrogen peroxide coagulated films, this study adds further evidence supporting the notion that increasing β-sheet content enhances ionic conductivity. The results of this investigation provides insights into how small amounts of rGO coupled with different coagulation agents can change the morphological, thermal, and conductive properties of cellulose and silk composites.

CRediT authorship contribution statement

Abneris Morales: Conceptualization, Methodology, Investigation, Supervision, Formal analysis, Visualization, Writing – original draft, Writing – review & editing. Sneha Seelam: Investigation, Writing – original draft, Writing – review & editing, Formal analysis. Stacy A. Love: Conceptualization, Formal analysis, Validation, Writing – review & editing. Sean M. O'Malley: Conceptualization, Methodology, Validation, Writing – review & editing. Xiao Hu: Conceptualization, Methodology, Funding acquisition, Validation, Writing – review & editing. David Salas-de la Cruz: Conceptualization, Methodology, Validation, Supervision, Writing – review & editing, Project administration, Visualization, Funding acquisition.

Declaration of competing interest

The authors declare the following financial interests/personal relationships which may be considered as potential competing interests: David Salas-de la Cruz reports financial support was provided by National Science Foundation. Xiao Hu reports financial support was provided by National Science Foundation. This information was provided in the acknowledgment sections.

Acknowledgements

We acknowledge the National Science Foundation (grants NSF-DMR 1809354, DMR 1809541 and CCMI-2037097) for providing the funding for this study, and the Rutgers-Camden Department of Chemistry. We would also like to thank Bailey Blessing, Rutgers University-Camden, NJ, Karleena Rybacki, Rutgers University-Camden, NJ, and Creston Singer, Rutgers University-Camden for technical assistance, and discussion. We extend a special thanks to Dr. Paul Heiney, Department of Physics and Astronomy, University of Pennsylvania-Philadelphia, PA for support and training on the DEXS. The DEXS System is supported by NSF-MRSEC (17-20530), NSF-MRI (17-25969), ARO DURIP (W911NF-17-1-02822), and the University of Pennsylvania. Salas-de la Cruz summer financial support was provided by NSF-CMMI (2037097) and NSF-DMR (2104376). Abneris financial support was provided by NSF-CMMI (2037097).

Appendix A. Supplementary data

Supplementary data to this article can be found online at https://doi.org/10.1016/j.ijbiomac.2023.123971.

References

- [1] A. Hadadi, J.W. Whittaker, D.E. Verrill, X. Hu, L. Larini, D. Salas-De La Cruz, A hierarchical model to understand the processing of polysaccharides/proteinbased films in ionic liquids, Biomacromolecules 19 (10) (2018) 3970–3982, https://doi.org/10.1021/acs.biomac.8b00903.
- [2] S.A. Love, E. Popov, K. Rybacki, X. Hu, D. Salas-de la Cruz, Facile treatment to finetune cellulose crystals in cellulose-silk biocomposites through hydrogen peroxide, Int. J. Biol. Macromol. 147 (2020) 569–575, https://doi.org/10.1016/j. ijbiomac.2020.01.100.

- [3] J. Stanton, Y. Xue, P. Pandher, L. Malek, T. Brown, X. Hu, D. Salas-de la Cruz, Impact of ionic liquid type on the structure, morphology, and properties of silkcellulose biocomposite materials, Int. J. Biol. Macromol. 108 (2018) 333–341, https://doi.org/10.1016/j.ijbiomac.2017.11.137.
- [4] B. Blessing, C. Trout, A. Morales, K. Rybacki, S.A. Love, G. Lamoureux, D. Salas-de la Cruz, Morphology and ionic conductivity relationship in silk/cellulose biocomposites, Polym. Int. 68 (9) (2019) 1580–1590, https://doi.org/10.1002/ pi.5860.
- [5] B. Blessing, C. Trout, A. Morales, K. Rybacki, S.A. Love, G. Lamoureux, D. Salas-De la Cruz, The impact of composition and morphology on ionic conductivity of silk/cellulose bio-composites fabricated from ionic liquid and varying percentages of coagulation agents, Int. J. Mol. Sci. 21 (13) (2020) 4695, https://doi.org/10.3390/iims21134605
- [6] D. Al-Shahrani, S.A. Love, D. Salas-De la Cruz, The role of reduced graphene oxide toward the self-assembly of lignin-based biocomposites fabricated from ionic liquids, Int. J. Mol. Sci. 19 (11) (2018) 3518, https://doi.org/10.3390/ ijms19113518.
- [7] M. Xu, Q. Huang, X. Wang, R. Sun, Highly tough cellulose/graphene composite hydrogels prepared from ionic liquids, Ind. Crop. Prod. 70 (2015) 56–63, https:// doi.org/10.1016/j.indcrop.2015.03.004.
- [8] V. Agarwal, G.W. Huber, W.C. Conner Jr., S.M. Auerbach, Simulating infrared spectra and hydrogen bonding in cellulose Iβ at elevated temperatures, J. Chem. Phys. 135 (13) (2011), 10B605, https://doi.org/10.1063/1.3646306.
- [9] M. Isik, H. Sardon, D. Mecerreyes, Ionic liquids and cellulose: dissolution, chemical modification, and preparation of new cellulosic materials, Int. J. Mol. Sci. 15 (7) (2014) 11922–11940, https://doi.org/10.3390/ijms150711922.
- [10] K.K. Sadasivuni, A. Kafy, H.C. Kim, H.U. Ko, S. Mun, J. Kim, Reduced graphene oxide filled cellulose films for flexible temperature sensor application, Synth. Met. 206 (2015) 154–161, https://doi.org/10.1016/j.synthmet.2015.05.018.
- [11] M. Jarvis, Cellulose stacks up, Nature 426 (6967) (2003) 611–612, https://doi.org/
- [12] A. Pinkert, K.N. Marsh, S. Pang, M.P. Staiger, Ionic liquids and their interaction with cellulose, Chem. Rev. 109 (12) (2009) 6712–6728, https://doi.org/10.1021/ cr9001947
- [13] G. Freddi, M. Romanò, M.R. Massafra, M. Tsukada, Silk fibroin/cellulose blend films: preparation, structure, and physical properties, J. Appl. Polym. Sci. 56 (12) (1995) 1537–1545, https://doi.org/10.1002/app.1995.070561203.
- [14] R.F. Pereira, K. Zehbe, C. Günter, T. Dos Santos, S.C. Nunes, F.A.A. Paz, V. de Zea Bermudez, Ionic liquid-assisted synthesis of mesoporous silk fibroin/silica hybrids for biomedical applications, ACS Omega 3 (9) (2018) 10811–10822, https://doi. org/10.1021/acsomega.8b02051.
- [15] X. Hu, P. Cebe, A.S. Weiss, F. Omenetto, D.L. Kaplan, Protein-based composite materials, Mater. Today 15 (5) (2012) 208–215, https://doi.org/10.1016/S1369-7021(12)70091-3.
- [16] D.M. Phillips, L.F. Drummy, D.G. Conrady, D.M. Fox, R.R. Naik, M.O. Stone, R. A. Mantz, Dissolution and regeneration of Bombyx mori silk fibroin using ionic liquids, J. Am. Chem. Soc. 126 (44) (2004) 14350–14351, https://doi.org/10.1021/ja046079f
- [17] S. Zhu, Y. Wu, Q. Chen, Z. Yu, C. Wang, S. Jin, G. Wu, Dissolution of cellulose with ionic liquids and its application: a mini-review, Green Chem. 8 (4) (2006) 325–327, https://doi.org/10.1039/b601395c.
- [18] B.A. Paren, R. Raghunathan, I.J. Knudson, J.L. Freyer, L.M. Campos, K.I. Winey, Impact of building block structure on ion transport in cyclopropenium-based polymerized ionic liquids, Polym. Chem. 10 (22) (2019) 2832–2839, https://doi. org/10.1039/c9pv00396g.
- [19] X. Yuan, G. Cheng, From cellulose fibrils to single chains: understanding cellulose dissolution in ionic liquids, Phys. Chem. Chem. Phys. 17 (47) (2015) 31592–31607, https://doi.org/10.1039/C5CP05744B.

- [20] S.B. Aziz, T.J. Woo, M.F.Z. Kadir, H.M. Ahmed, A conceptual review on polymer electrolytes and ion transport models, J.Sci.Adv.Mater.Devices 3 (1) (2018) 1–17, https://doi.org/10.1016/j.jsamd.2018.01.002.
- [21] J.S. Kumar, A.R. Subrahmanyam, M.J. Reddy, U.S. Rao, Preparation and study of properties of polymer electrolyte system (PEO+ NaClO3), Mater. Lett. 60 (28) (2006) 3346–3349, https://doi.org/10.1016/j.matlet.2006.03.015.
- [22] Y. Zhang, C. Wu, S. Guo, J. Zhang, Interactions of graphene and graphene oxide with proteins and peptides, Nanotechnol. Rev. 2 (1) (2013) 27–45, https://doi.org/ 10.1515/ntrev-2012-0078.
- [23] V.B. Mohan, R. Brown, K. Jayaraman, D. Bhattacharyya, Characterization of reduced graphene oxide: effects of reduction variables on electrical conductivity, Mater. Sci. Eng. B 193 (2015) 49–60, https://doi.org/10.1016/j. pseb. 2014.11.002
- [24] B.R. Singh, D.B. DeOliveira, F.N. Fu, M.P. Fuller, Fourier transform infrared analysis of amide III bands of proteins for the secondary structure estimation, in: Biomolecular Spectroscopy III Vol. 1890, SPIE, 1993, May, pp. 47–55, https://doi. org/10.1117/12.145242.
- [25] S. Garcia-Granda, J. Montejo-Bernardo, X-ray absorption and diffraction | X-ray diffraction powder, in: Encyclopedia of Analytical Science, 2005, pp. 389–397, https://doi.org/10.1016/b0-12-369397-7/00671-3.
- [26] S.A. Love, X. Hu, D. Salas-de la Cruz, Controlling the structure and properties of semi-crystalline cellulose/silk-fibroin biocomposites by ionic liquid type and hydrogen peroxide concentration, Carbohydr.Polym.Technol.Applic. 3 (2022), 100193, https://doi.org/10.1016/j.carpta.2022.100193.
- [27] D. Salas-De La Cruz, M.D. Green, Y. Ye, Y.A. Elabd, T.E. Long, K.I. Winey, Correlating backbone-to-backbone distance to ionic conductivity in amorphous polymerized ionic liquids, J. Polym. Sci. B Polym. Phys. 50 (5) (2012) 338–346, https://doi.org/10.1002/polb.23019.
- [28] S. Hindi, The interconvertibility of cellulose's allomorphs, Int. J. Innov. Res. Sci. Eng. Technol 6 (2017) 715–722, https://doi.org/10.15680/ LIBSET.2017.0601125.
- [29] M.N. Costa, B. Veigas, J.M. Jacob, D.S. Santos, J. Gomes, P.V. Baptista, R. Martins, J. Inácio, E. Fortunato, A low cost, safe, disposable, rapid and self-sustainable paper-based platform for diagnostic testing: lab-on-paper, Nanotechnology 25 (9) (2014), 094006, https://doi.org/10.1088/0957-4484/25/9/094006.
- [30] F. Wang, S.J. Aravind, H. Wu, J. Forys, V. Venkataraman, K. Ramanujachary, X. Hu, Tunable green graphene-silk biomaterials: mechanism of protein-based nanocomposites, Mater. Sci. Eng. C 79 (2017) 728–739, https://doi.org/10.1016/j. msec.2017.05.120.
- [31] J. Stanton, Y. Xue, J.C. Waters, A. Lewis, D. Cowan, X. Hu, D.S.D. la Cruz, Structure–property relationships of blended polysaccharide and protein biomaterials in ionic liquid, Cellulose 24 (4) (2017) 1775–1789, https://doi.org/ 10.1007/s10570-017-1208-y.
- [32] S.H. Kim, C.M. Lee, K. Kafle, Characterization of crystalline cellulose in biomass: basic principles, applications, and limitations of XRD, NMR, IR, Raman, and SFG, Korean J. Chem. Eng. 30 (12) (2013) 2127–2141, https://doi.org/10.1007/ s11814-013-0162-0.
- [33] A.D. French, M. Santiago Cintrón, Cellulose polymorphy, crystallite size, and the Segal Crystallinity Index, Cellulose 20 (1) (2013) 583–588, https://doi.org/ 10.1007/s10570-012-9833-v.
- [34] S. Nam, A.D. French, B.D. Condon, M. Concha, Segal crystallinity index revisited by the simulation of X-ray diffraction patterns of cotton cellulose Iβ and cellulose II, Carbohydr. Polym. 135 (2016) 1–9, https://doi.org/10.1016/j. carbool.2015.08.035.
- [35] J. Han, C. Zhou, A.D. French, G. Han, Q. Wu, Characterization of cellulose II nanoparticles regenerated from 1-butyl-3-methyllimidazolium chloride, Carbohydr. Polym. 94 (2) (2013) 773–781, https://doi.org/10.1016/j. carbpol.2013.02.003.